



# Ceria-doped and TiO<sub>2</sub> nanocomposite coating on multiwalled carbon nanotubes for the photocatalytic remediation of agro-industrial wastewaters

D. Wilson<sup>b</sup>, W. Wang<sup>b</sup>, Rodrigo J.G. Lopes<sup>a,\*</sup>

<sup>a</sup> CIEPQPF – Centro de Investigação em Engenharia dos Processos Químicos e Produtos da Floresta, GERSE – Group on Environmental, Reaction and Separation Engineering, Department of Chemical Engineering, University of Coimbra, Rua Sílvio Lima, Polo II – Pinhal de Marrocos, 3030-790 Coimbra, Portugal

<sup>b</sup> MSC Catalysis Research Laboratories, California Institute of Technology, Pasadena, CA 91135, United States

## ARTICLE INFO

### Article history:

Received 7 February 2012

Received in revised form 24 April 2012

Accepted 27 April 2012

Available online 5 May 2012

### Keywords:

Photo-oxidation

Phenolic pollutants

CNT

TiO<sub>2</sub>

CeO<sub>2</sub>

FESEM

TEM

XRD

## ABSTRACT

Aiming to gain further insights into the heterogeneous catalysis of carbon nanotubes (CNTs), several catalysts have been investigated by embedding TiO<sub>2</sub> and CeO<sub>2</sub> into CNTs for the photo-oxidation of high-strength liquid pollutants. First, the CNT/TiO<sub>2</sub>–CeO<sub>2</sub> nanocomposites were synthesized by the surfactant wrapping sol–gel technique with titanium isopropoxide precursor. The photocatalytic activity in parent compound depletion was evaluated comparatively with the photocatalytic efficiency in total organic carbon (TOC) abatement at UV–254 and 420 nm. Here, the higher photodegradation efficiencies in pollutant (88.2%) and TOC (61.9%) were achieved with the CNT<sub>0.5</sub>/(TiO<sub>2</sub>)<sub>9</sub>–(CeO<sub>2</sub>)<sub>0.5</sub> catalyst. Second, the nanocomposites have been characterized by FESEM and TEM techniques indicating a highly heterogeneous porous structure with equivalent nanotube length and wall thickness as well as confirming the existence of a continuous titanium and cerium oxide layer coating the surface of CNTs. Afterwards, the XRD structure and chemical composition has been used to query the effect of the calcination temperature. The CNT/TiO<sub>2</sub>–CeO<sub>2</sub> nanocomposites exhibited remarkable differences concerning the crystalline morphology and the BET/porosity analysis pointed out the presence of mesopores in the nanoparticle matrix. Finally, several sequential mineralization trials were accomplished by recycling the most active catalyst, and CNT<sub>0.5</sub>/(TiO<sub>2</sub>)<sub>9</sub>–(CeO<sub>2</sub>)<sub>0.5</sub> has preserved 61% of TOC conversion for long-term photo-oxidation experiments.

© 2012 Elsevier B.V. All rights reserved.

## 1. Introduction

Bisphenols, catechols, phenol ethers, alkylphenols, trihydroxybenzenes, and hydroxybiphenyls belong to a priority list of toxic organic compounds listed by EPA in water pollution directives. Among the known and threatened releases of hazardous substances, modern wastewater management technologies should encompass a broad range of efforts that promote effective and responsible water use, treatment, and secure disposal. Having legislated on point and non-point categories of water pollution, local governments and non-governmental organizations encouraged and regulated the discharges into surface waters by involving green infrastructure mechanisms and guidelines for wastewater/stormwater sustainability.

The above-mentioned compounds often contaminated the natural water bodies and are produced in the petrochemical, pharmaceutical, pesticide, dye and agro-industries. Phenol derivatives

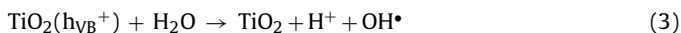
are characterized by their toxicity, difficulty and persistency at the time of water decontamination. Consequently, highly efficient techniques such as photocatalytic and sonochemical degradation, Fenton oxidation, ozonation, microwave irradiation, supercritical water oxidation and wet air oxidation are advanced oxidation techniques, which degrade organic compounds to harmless final products using appropriate catalysts [1–6].

In order to minimize the operational costs of advanced technologies for wastewater treatment, photocatalytic oxidation is envisaged as a promising route to completely degrade toxic pollutants by consuming less chemicals, energy, and time in comparison to conventional processes such as the biological oxidation and adsorption technologies [3]. As an advanced oxidation process, the photodegradation of high-strength liquid pollutants comprises the generation of hydroxyl radical (OH•), which is a non-selective and powerful oxidizing agent for the remediation of hazardous compounds. Photogenerated holes are created after irradiating TiO<sub>2</sub> particles with UV light (Eq. (1)) so the hydroxyl radicals are mostly engendered in the oxidation of OH<sup>–</sup> or H<sub>2</sub>O (Eqs. (2) and (3)). Hence, the photogenerated holes are primarily responsible for the destruction of phenol-like pollutants as long as the oxygen is used as an

\* Corresponding author. Tel.: +351 239798723; fax: +351 239798703.

E-mail address: [rodrigo@eq.uc.pt](mailto:rodrigo@eq.uc.pt) (R.J.G. Lopes).

efficient electron trap (Eq. (4)) by avoiding the recombination of electrons and photogenerated holes. These photocatalytic events can be chemically expressed as follows



Apart from the application of photocatalysts as semiconductors which was restricted to the reassembling of the generated photo-holes and photo-electrons, there has been an increasing interest on how to increase the photocatalytic efficiency [7–9]. These literature reports have focused on the chemical oxidation concept performed by photo-holes from the semiconductor, and further recombination occurs with the loss of holes that possibly otherwise have improved the pollutant degradation [10,11]. Here, the net transfer of photo-generated electrons and holes between the conduction and valence bands of semiconductors plays a major role at the time of promoting and intensifying the photocatalytic efficiency. Commonly, a straightforward method to accomplish such a task was to increase the surface area of  $\text{TiO}_2$ , the coupling of  $\text{TiO}_2$  with transition metals and/or semiconductors, and the generation of reactive-ready structures to induce space-charge separation events [9]. An alternative route to improve the photocatalytic efficiency of  $\text{TiO}_2$  may be undertaken by embedding inorganic/organic, ceramic supports such as alumina, zeolites, silica, and clay [11] or including  $\text{SnO}_2$  and platinum nanoparticles [12–14]. However, scarce results on this subject need to be comprehensively investigated for the subsequent development of novel materials for modifying  $\text{TiO}_2$ .

In the realm of nanocatalysis, carbon nanotubes (CNT) have received particular attention mainly due to their special morphology, distinctive mechanical and remarkable electronic/semiconducting properties [15]. Apart from increasing the photocatalytic activity of  $\text{TiO}_2$ , the surface area of CNT is significantly lower than that of activated carbon so the adsorption is not the only factor for increasing the photocatalytic activity of  $\text{TiO}_2$  by CNT [16]. As carbon nanotubes are one-dimensional carbon-based molecules arranged in a nanocylinder structure, they can expeditiously conduct electricity at room temperature with negligible resistance [17]. Additionally, this phenomenon also accounts for the electrons generated by the UV irradiation which migrate to the surface of  $\text{TiO}_2$ , and are rapidly transported in CNT coupled with  $\text{TiO}_2$ .

Aiming to advance the photocatalytic efficiency of  $\text{TiO}_2$ , here we evaluate how the environmental detoxification of phenol-like pollutants may be promoted by embedding  $\text{CeO}_2$  in the CNT/ $\text{TiO}_2$  catalytic framework. To the best of our knowledge, cerium oxides have not been investigated in conjunction with carbon nanotubes/titanium oxides. As transition metals such as cerium are recognized to enhance the oxidant storage and release by improving its further mobility, the modification of CNT/ $\text{TiO}_2$  by  $\text{CeO}_2$  will serve as an alternative benchmark. In this regard, the purpose of such approach is twofold: to characterize thoroughly cerium and titanium oxides by FESEM, TEM, XRD, and BET techniques when integrated with carbon nanotubes, and to evaluate systematically the detoxification efficiency of biologically refractory agro-industrial pollutants by photocatalytic oxidation.

## 2. Experimental

### 2.1. Materials and synthesis of CNT/ $\text{TiO}_2$ – $\text{CeO}_2$

The  $\text{TiO}_2$  was obtained from the Merck Co. and is mainly characterized by the anatase type with a specific surface area of  $5 \text{ m}^2/\text{g}$ .

The CNTs were produced by chemical vapor deposition through the pyrolysis of methane gas on particles of nickel. The CNT/ $\text{TiO}_2$ – $\text{CeO}_2$  nanocomposites were synthesized by the surfactant wrapping sol–gel technique with titanium isopropoxide (Fluka, >99%) and further functionalized with sodium dodecylbenzenesulfonate. This surface modification agent allows obtaining a homogeneous and mesoporous anatase layer over the carbon nanotubes. Raw multi-wall CNTs with 10–200 nm in diameter and 1–50  $\mu\text{m}$  in length have been dispersed into the aqueous solution of surface functionalizing agent (1 wt.%). After sonication, the CNTs concentration was 31 g/L and the suspension was subsequently mixed with 15 mL ethanol (Aldrich, >90%) for 20 min. The titanium precursor with a pre-calculated amount has been mixed with glacial acetic acid (Acros, aldehyde free) and ethanol for 15 min to give a transparent solution. The solution of the functionalizing agent was added into the suspension of carbon nanotubes under continuous stirring conditions for 3 h. The hydrolysis of the titanium precursor was stopped by adding dropwise an aqueous ammonia solution (Acros, 30%). The resulting suspension was then successively centrifuged by five cycles and washed with ethanol. The sample was dried at  $80^\circ\text{C}$  for 30 min to produce crystalline carbon nanotubes/titanium oxide catalysts.

$\text{CeO}_2$  nanoparticles were deposited on carbon nanotubes by means of electrodeposition process with  $\text{CeCl}_3 \cdot 7\text{H}_2\text{O}$  (0.05 M) in ethanol as the plating solution. Preliminary to the electrodeposition, the CNT/ $\text{TiO}_2$  was immersed in the deposition solution for 2 h in order to allow the diffusion of the plating solution into the multiwall carbon nanotubes. The electrodeposition was carried out at  $-15 \text{ V}$  (vs.  $\text{Ag}/\text{AgCl}$ ) for 2 min and terminated after the total charge achieving  $50 \text{ mC}/\text{cm}^2$ . Different nanocomposites with molar proportions were prepared as follows:  $\text{CNT}_{0.5}/(\text{TiO}_2)_9-(\text{CeO}_2)_{0.5}$ ,  $\text{CNT}_1/(\text{TiO}_2)_8-(\text{CeO}_2)_1$ ,  $\text{CNT}_2/(\text{TiO}_2)_7-(\text{CeO}_2)_1$ ,  $\text{CNT}_1/(\text{TiO}_2)_9$ ,  $\text{TiO}_2$ , CNT. From a benchmark point of view, electrodeposition has also been used to produce pure  $\text{CeO}_2$  films with a final dumped charge of  $200 \text{ mC}/\text{cm}^2$ . These catalytic formulations were cured at different calcination temperatures within the range 300, 500,  $700^\circ\text{C}$  for 1 h formerly to the morphological, structural and chemical characterization analysis. The calcination temperature range enables the selection of the optima treatment conditions to attain a high-level of  $\text{TiO}_2$  crystallization and circumventing the loss of carbon from the core of the CNT/ $\text{TiO}_2$  structure at higher calcination temperatures.

### 2.2. Photoreactor and oxidation procedure

The photocatalytic oxidations were performed in a 2 L hollow cylindrical glass reactor. The UV lamp (Philips) with 8 W emitting at 254 and 420 nm was located inside the inner tube made of quartz. The experimental runs were controlled at  $25^\circ\text{C}$  and 7 mg/L dissolved oxygen and stirred continuously at 250 rpm. Six phenol-like compounds have been used to replicate the biologically refractory behavior of agro-industrial processing wastewaters, namely: syringic, vanillic, 3,4,5-trimethoxybenzoic, veratric, protocatechuic and *trans*-cinnamic acid (1200 mg/L, 200 mg/L for each compound). The suspended solids in the UV/CNT/ $\text{TiO}_2$ – $\text{CeO}_2$  system were separated by centrifugation at 4000 rpm for 15 min, and then filtered through a  $0.22 \mu\text{m}$  filter (Millipore). For comparison purposes, adsorption and direct photolysis were accomplished to evaluate the abatement efficiency of phenol-like pollutants across all of photo-oxidation experiments.

The influence of CNTs on the photocatalytic activity of  $\text{TiO}_2$ – $\text{CeO}_2$  was investigated by adding  $\text{TiO}_2$ – $\text{CeO}_2$  and CNTs in different molar ratios:  $\text{CNT}_{0.5}/(\text{TiO}_2)_9-(\text{CeO}_2)_{0.5}$ ,  $\text{CNT}_1/(\text{TiO}_2)_8-(\text{CeO}_2)_1$ ,  $\text{CNT}_2/(\text{TiO}_2)_7-(\text{CeO}_2)_1$ ,  $\text{CNT}_1/(\text{TiO}_2)_9$ ,  $\text{TiO}_2$ , CNT. The mixture of phenolic acids was mixed with these nanocomposites in the dark for 1 h to promote the hydration

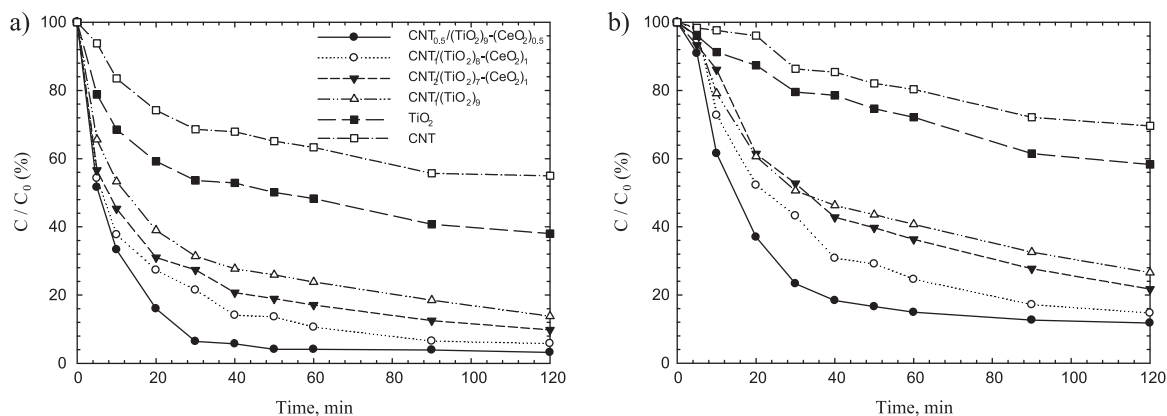


Fig. 1. Parent compound depletion as a function of reaction time for (a) UV-254 nm and (b) 420 nm at  $T = 25^\circ\text{C}$  with the 0.5 g/L laboratory-made catalysts.

conditions in advance to the UV irradiation at 254 and 420 nm with an intensity of  $4\text{ mW/cm}^2$ . The photocatalytic experiments were monitored for individual pollutant oxidation and total organic carbon mineralization by sampling 5 mL of reaction mixture. The photocatalytic abatement of phenolic acids was quantified using a HACH spectrophotometer DR-4000V. After each photocatalytic experiment, the suspension was centrifuged and further filtered to evaluate the total organic carbon concentration.

### 2.3. Analytical techniques

The morphology of the CNT/TiO<sub>2</sub>–CeO<sub>2</sub> nanocomposites was investigated using field emission scanning electron microscopy (FESEM, JEOL JSM-6700F). The microstructure and composition were analyzed by recording transmission electron microscopy (TEM) measurements on a TECNAI G<sup>2</sup> 20 S-TWIN transmission electron microscopy. It allows flexible high tension values (20, 40, 80, 120, 160, 200 kV) and use LaB<sub>6</sub> or W emitter as the electron source. The TEM point and line resolutions are 0.24 and 0.144 nm, respectively, whereas the minimum focus step is 1.8 nm. The TEM magnification range is  $25\times$  to  $1030\times$  while the STEM magnification range is  $100\times$  to  $5\text{M}\times$ . For these TEM analyses, the specimens were prepared by suspending solid samples and further ultrasonicated in ethanol for 30 min.

The textural properties and nitrogen sorption isotherms of CNT/TiO<sub>2</sub>–CeO<sub>2</sub> were determined by the volumetric technique at 77 K using nitrogen by a Micrometrics ASAP 2010 sorptometer. The samples were preliminary submitted to over-drying at  $80^\circ\text{C}$  and evacuated overnight under vacuum condition. The surface area was quantified using Brunauer–Emmett–Teller (BET) surface analysis based on adsorption data in the partial pressure ( $P/P_0$ ) range 0.05–0.95. The amount of nitrogen adsorbed at  $P/P_0 = 0.995$  was used to calculate the total pore volume and the average pore size was found from the adsorption data by Barrett–Joyner–Halenda (BJH) porosity method.

The nanocomposite crystallinity was characterized by powder X-ray diffraction in a Philips EXPERT  $\theta$ – $2\theta$  X-ray diffractometer with Cu K $\alpha$  radiation ( $\lambda = 1.53\text{ \AA}$ ) from  $20^\circ$  to  $120^\circ$   $2\theta$  at a scanning speed of  $0.03^\circ\text{ s}^{-1}$ . The X-ray tube voltage and current were set at 35 kV and 45 mA, respectively. The line broadening of anatase TiO<sub>2</sub> reflection plane ( $2\theta = 48^\circ$ ) has been used to probe the crystallite size pointing out that there was negligible interference from carbon nanotubes.

The concentration of phenol-like compounds in aqueous solution was followed by HPLC (Finnigan P4000 Model) reversed phase column (RESTEK Pinnacle II, C18) with a particle size of  $5\text{ }\mu\text{m}$ , the length of 250 mm. The mobile phase of (acetonitrile – 60 vol.%; water – 35 vol.%; acetic acid – 5 vol.%) flowed at  $0.5\text{ mL min}^{-1}$  in

the chromatographic column with 4.5 mm ID. Additionally, the pollutant concentration was quantified with a UV 6000LP detector at 220 nm. pH was monitored along the reactions with a HANNA instrument-HI8711E. TOC was measured with a Shimadzu 5050 TOC Analyser, which operates based on the combustion/nondispersive infrared gas analysis method. The parameter uncertainty in TOC measurement, quoted as the deviation of three separate measurements, was never larger than 2% for the range of the TOC concentrations.

## 3. Results

### 3.1. Photocatalytic activity in parent compounds depletion

The catalytic activity of laboratory-made CNT/TiO<sub>2</sub>–CeO<sub>2</sub> catalysts was evaluated in terms of abatement efficiency of the phenolic acids mixture. The normalized concentration is shown in Fig. 1 under different irradiation wavelengths. Fig. 1a plots the photodegradation of liquid pollutants at UV-254 nm and  $T = 25^\circ\text{C}$  with different molar proportions for the nanocomposites. After 30 min of reaction time, the conversion profile was 93.6, 78.5, 72.6, 68.6, 46.4, and 31.4% for CNT<sub>0.5</sub>/(TiO<sub>2</sub>)<sub>9</sub>–(CeO<sub>2</sub>)<sub>0.5</sub>, CNT<sub>1</sub>/(TiO<sub>2</sub>)<sub>8</sub>–(CeO<sub>2</sub>)<sub>1</sub>, CNT<sub>2</sub>/(TiO<sub>2</sub>)<sub>7</sub>–(CeO<sub>2</sub>)<sub>1</sub>, CNT<sub>1</sub>/(TiO<sub>2</sub>)<sub>9</sub>, TiO<sub>2</sub>, and CNT, respectively. As can be seen, the higher rates of decontamination were attained for all nanocomposites during the first 30 min and slowed down after 1 h as follows: 95.9, 89.4, 82.9, 76.2, 51.7, and 36.7%. Among these conversion profiles, the CNT and TiO<sub>2</sub> catalysts gave the worst removal efficiencies whereas the CNT/TiO<sub>2</sub>–CeO<sub>2</sub> revealed worthy properties regarding the superior reaction rates with the subsequent conversion data after 2 h 96.8, 94.2, 90.2, 86.2, 62.0, and 45.0% for CNT<sub>0.5</sub>/(TiO<sub>2</sub>)<sub>9</sub>–(CeO<sub>2</sub>)<sub>0.5</sub>, CNT<sub>1</sub>/(TiO<sub>2</sub>)<sub>8</sub>–(CeO<sub>2</sub>)<sub>1</sub>, CNT<sub>2</sub>/(TiO<sub>2</sub>)<sub>7</sub>–(CeO<sub>2</sub>)<sub>1</sub>, CNT<sub>1</sub>/(TiO<sub>2</sub>)<sub>9</sub>, TiO<sub>2</sub>, and CNT, respectively. Therefore, the integration of the lanthanide to the carbon nanotube/titanium oxide framework promotes the electron transport capacity of CNT. Bearing in mind that carbon nanotubes have been extensively used for the preparation with conjugated polymers in light-emitting diodes, field effect transistors and photovoltaic devices, here the photo-induced charge transfer occurs in the electronic interaction as also reported between polymer chains and CNT. Thus, the recombination of electron/hole promoted by TiO<sub>2</sub> under UV light plays a major role. This fact is partly ascribed to the considerable differences attained when comparing the conversion profiles, so the strong interaction between TiO<sub>2</sub>–CeO<sub>2</sub> and CNT explains the electron transfer of these nanocomposites by decreasing the electron/hole reassembly and enhancing the photon efficiency.

Fig. 1b illustrates the photo-oxidation profiles at 420 nm and  $T = 25^\circ\text{C}$  with different molar proportions for the CNT/TiO<sub>2</sub>–CeO<sub>2</sub>



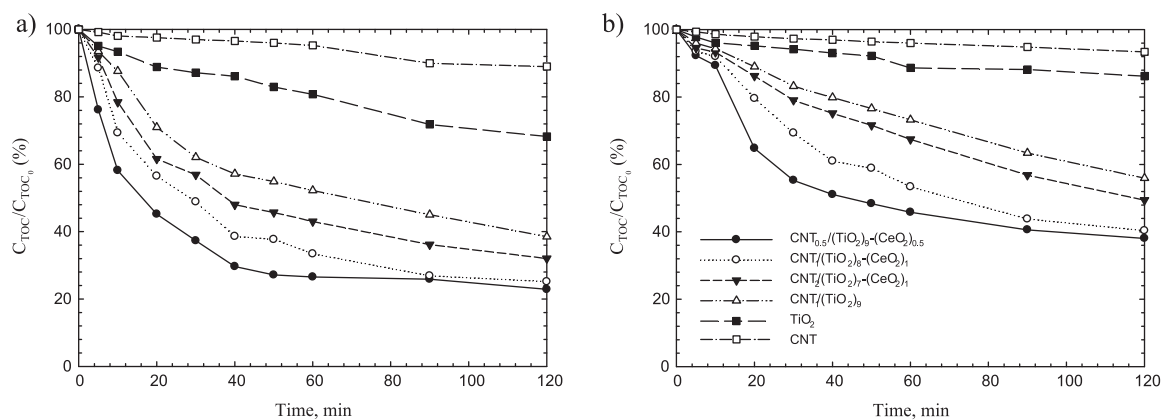


**Fig. 2.** Normalized total organic carbon concentration as a function of time for (a) UV-254 nm and (b) 420 nm at  $T = 25^\circ\text{C}$  with the 0.5 g/L laboratory-made catalysts.

nanocomposites. As can be seen the removal efficiencies decreased significantly during the first 30 min to 76.7, 56.8, 47.3, 49.4, 20.4, and 13.6% for  $\text{CNT}_{0.5}/(\text{TiO}_2)_9-(\text{CeO}_2)_{0.5}$ ,  $\text{CNT}_1/(\text{TiO}_2)_8-(\text{CeO}_2)_1$ ,  $\text{CNT}_2/(\text{TiO}_2)_7-(\text{CeO}_2)_1$ ,  $\text{CNT}_1/(\text{TiO}_2)_9$ ,  $\text{TiO}_2$ , and CNT, respectively. The photodegradation conversions corresponding to the

influence of CNT concentration confirmed that superior detoxification rates in photoactivity were most significant in the  $\text{CNT}_{0.5}/(\text{TiO}_2)_9-(\text{CeO}_2)_{0.5}$  mainly due to the best compromise between the cerium and titanium oxide concentration. Indeed, the conversion profile obtained after 2 h of reaction time was 88.2,

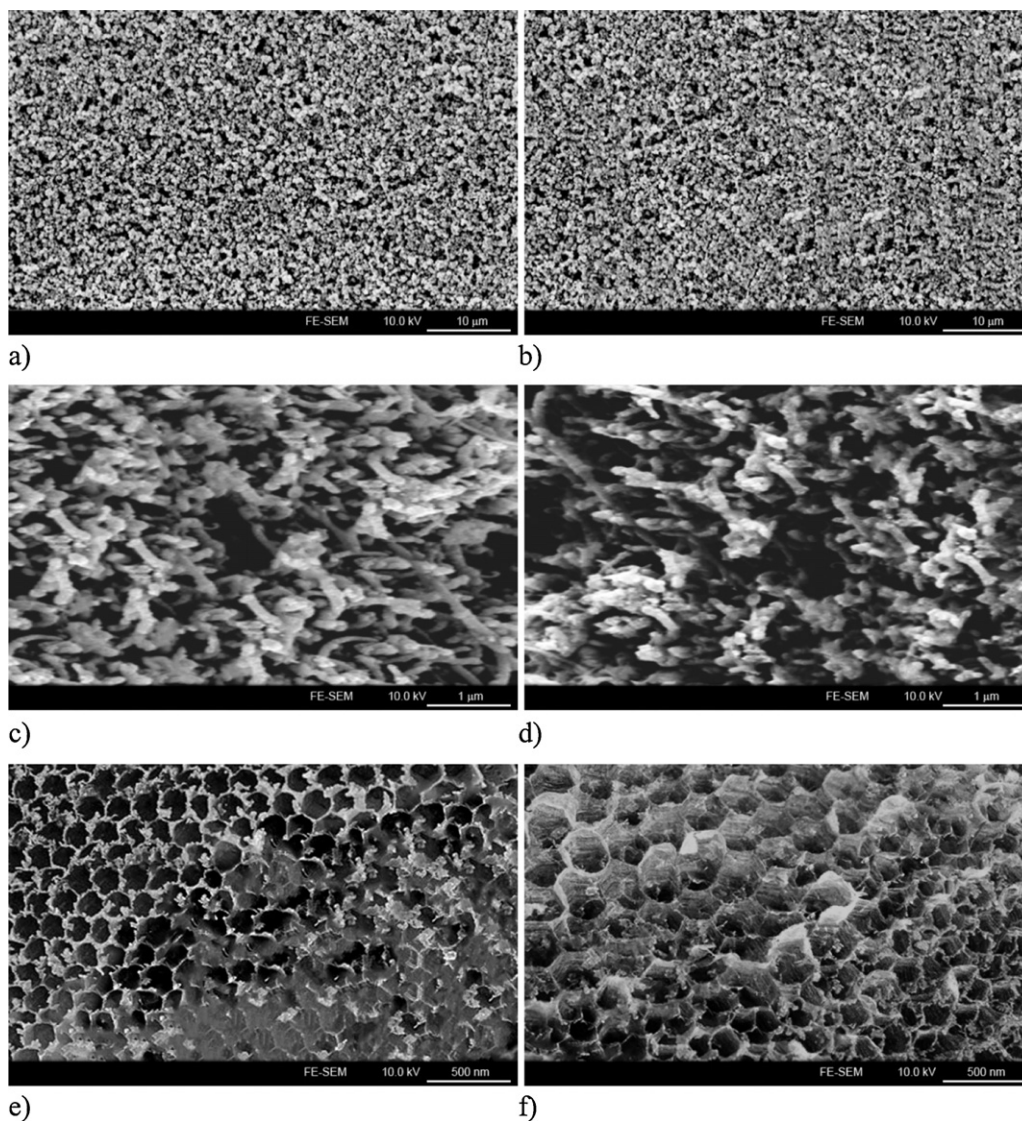


**Fig. 3.** Field emission scanning electron microscopy photographs of (a, c, e) fresh and (b, d, f) used  $\text{CNT}_{0.5}/(\text{TiO}_2)_9-(\text{CeO}_2)_{0.5}$  catalyst.

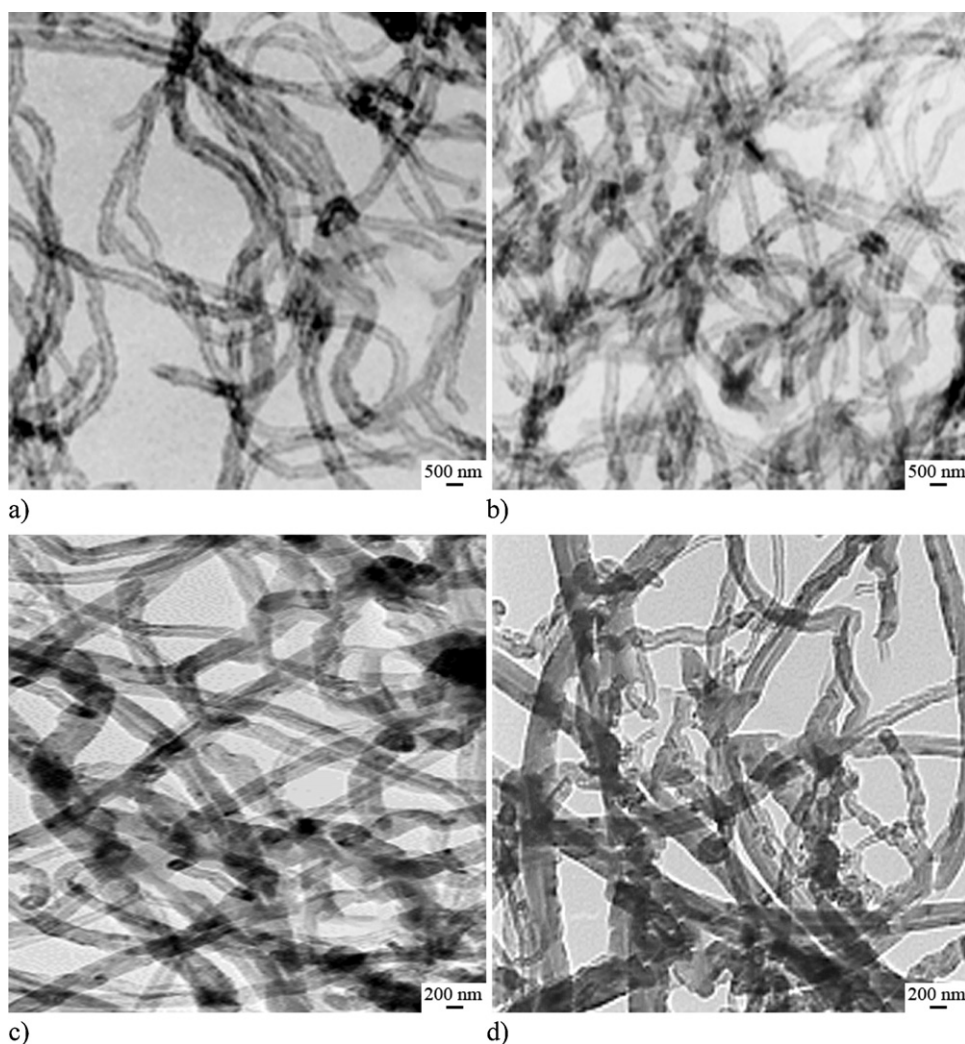


**Fig. 4.** Transmission electron microscopy patterns of (a–c) fresh and (b–d) used  $\text{CNT}_{0.5}/(\text{TiO}_2)_9-(\text{CeO}_2)_{0.5}$  catalyst.

85.3, 78.3, 73.4, 41.7, and 30.3%. Provided that multiwall carbon nanotubes may significantly inhibit electron/hole recombination, the two least efficient nanocomposites were not able to efficiently absorb UV radiation, thereby reducing electrons and holes production. The photodegradation profiles depicted in Fig. 1b unveiled that the photoactivity of  $\text{CNT}/\text{TiO}_2-\text{CeO}_2$  nanocomposites were reduced at 420 nm in comparison to Fig. 1a. The weaker decontamination efficiencies of CNT and  $\text{TiO}_2$ -single systems gave rise to the electron transfer phenomena, which occurred under visible light making possible to perform the photo-oxidation by using the solar radiation.

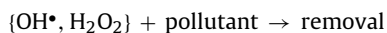
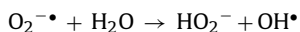
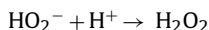
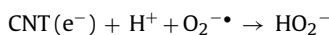
### 3.2. Photocatalytic efficiency in TOC abatement

The photodegradation activity of the phenol-like pollutants was quantified in term of total organic carbon abatement. Fig. 2a shows the removal efficiencies attained with different nanocomposites at UV-254 nm and  $T=25^\circ\text{C}$ . During the first 30 min, the TOC conversions were 62.7, 51.1, 43.1, 37.9, 12.8, and 3.0% for  $\text{CNT}_{0.5}/(\text{TiO}_2)_9-(\text{CeO}_2)_{0.5}$ ,  $\text{CNT}_1/(\text{TiO}_2)_8-(\text{CeO}_2)_1$ ,  $\text{CNT}_2/(\text{TiO}_2)_7-(\text{CeO}_2)_1$ ,  $\text{CNT}_1/(\text{TiO}_2)_9$ ,  $\text{TiO}_2$ , and CNT, respectively. The  $\text{CNT}/\text{TiO}_2-\text{CeO}_2$  catalysts were the most active toward the mineralization of the phenolic wastewater so the final TOC conversions were 77.1, 74.8, 68.0, 61.5, 31.7, and 11.0%. Likewise, the photo-oxidation profiles obtained at 420 nm and  $T=25^\circ\text{C}$  are

plotted in Fig. 2b. As can be seen, the detoxification efficiencies decreased considerably after 30 min reaction time as follows: 44.7, 30.7, 20.9, 16.7, 5.8, and 2.7% for  $\text{CNT}_{0.5}/(\text{TiO}_2)_9-(\text{CeO}_2)_{0.5}$ ,  $\text{CNT}_1/(\text{TiO}_2)_8-(\text{CeO}_2)_1$ ,  $\text{CNT}_2/(\text{TiO}_2)_7-(\text{CeO}_2)_1$ ,  $\text{CNT}_1/(\text{TiO}_2)_9$ ,  $\text{TiO}_2$ , and CNT, respectively. In fact, the total organic carbon conversions had slightly increased after 2 h: 61.9, 59.7, 50.6, 44.0, 13.8, and 6.6%. Consequently, the photo-oxidation are not likely feasible for the pollution abatement of phenol-like hazardous species without the application of an active catalyst such as  $\text{CNT}/\text{TiO}_2-\text{CeO}_2$  nanocomposites. Additionally, the toxicity of the phenolic wastewater was monitored to characterize how risky were the parent compounds. A high biodegradability improvement generally occurred after the application of the chemical oxidation process when compared with the case of the initial effluent. Indeed, luminescence techniques were applied to infer about the raw and depurated wastewater ecological impact by determining the samples  $\text{EC}_{20}$  and  $\text{EC}_{50}$ . For all the experiments, a toxicity reduction takes place by pulling off the  $\text{EC}_{50}$  values out of the apparatus scope, which means that even the undiluted samples cannot produce light inhibition of 50% of the *Vibrio fischeri* population.

The parent compound and TOC concentration profiles gave further insights into the reaction mechanism. As an electron is transferred from  $\text{TiO}_2$  to CNT, the reassembly is negatively affected and the case scenario evolves with additional electrons being transferred from  $\text{TiO}_2$  to CNT so the  $e/h^+$  recombination is even reduced

accordingly. Having carried out the photo-oxidation experiments with aqueous solutions, hydrogen ions and water molecules participate in this mechanism as follows:



By adding a supplementary amount of oxygen, electrons reacted with the oxidant in the carbon nanotubes to generate excited oxyhydrogen radicals. The reassembly of these photo-produced electrons and holes in  $\text{TiO}_2$ - $\text{CeO}_2$  nanocomposites is noticeably stronger as the oxidant concentration increases and concomitantly promotes the photodegradation efficiencies. Specifically, when CNT are integrated with titanium and cerium oxides, the absorption edge occurs at shorter UV wavelength so the band gaps for  $\text{TiO}_2$ - $\text{CeO}_2$  and  $\text{CNT}/\text{TiO}_2$ - $\text{CeO}_2$  have been quantified as 3.19 and 3.57 electron-volts, as similarly reported elsewhere [18]. Provided that a powerful redox capacity is characterized by a larger band gap, and the chemisorption of water onto the surface of carbon nanotubes/titanium oxide composites have pointed out that additional hydroxyl groups are produced, the photo-oxidation efficiency are enhanced for all  $\text{CNT}/\text{TiO}_2$ - $\text{CeO}_2$  composites.

### 3.3. FESEM and TEM morphological characterization

Representative field emission scanning electron microscopy photographs have been recorded for  $\text{CNT}/\text{TiO}_2$ - $\text{CeO}_2$  nanocomposite and are depicted in Fig. 3 for fresh and used  $\text{CNT}_{0.5}/(\text{TiO}_2)_9-(\text{CeO}_2)_{0.5}$  catalyst. Different magnifications corresponding to 10  $\mu\text{m}$ , 1  $\mu\text{m}$  and 500 nm enable a morphological characterization as illustrated by Fig. 3ab, cd and ef, respectively. The formation of multiwall nanotube arrays on the surface of titanium and cerium oxides depends upon the chemical dissolution and electrochemical etching stages. As the morphology and structure of carbon nanotubes is dictated by the interaction between these phenomena, the photocatalytic activity of nanocomposites was affected accordingly. According to the FESEM images shown in Fig. 3, the nanocomposite revealed a porous structure and the thickness is smaller than 1  $\mu\text{m}$ . Several anodization parameters have been reported in the literature to compare the sol-gel method with the anodic oxidation synthesis. Contrarily to the nanotubes arrays anodized at low voltages, the  $\text{CNT}_{0.5}/(\text{TiO}_2)_9-(\text{CeO}_2)_{0.5}$  unveiled a well-developed porous microstructure and presenting

individual and ordered alignments. The surfactant wrapping sol-gel technique has been investigated for the preparation of  $\text{CNT}/\text{TiO}_2$ - $\text{CeO}_2$  nanocomposites with different wall thicknesses. A highly heterogeneous porous structure with equivalent nanotube length was obtained for a thicker wall of  $\sim 100$  nm. Comparatively to the effect of lower anodization temperature, the synthesis of  $\text{CNT}/\text{TiO}_2$ - $\text{CeO}_2$  nanocomposites with higher wall thicknesses gave rise to the concurrent reactions of chemical dissolution and electrochemical etching of titanium in the formation of the nanotube arrays under such an anodic conditions.

The TEM patterns of the  $\text{CNT}/\text{TiO}_2$ - $\text{CeO}_2$  nanocomposites are shown in Fig. 4 for fresh (ac) and used (bd)  $\text{CNT}_{0.5}/(\text{TiO}_2)_9-(\text{CeO}_2)_{0.5}$  catalyst. As can be seen, these images confirmed the presence of a continuous layer coating, which covers almost completely the surface of carbon nanotubes. In addition, the diameter of the raw nanotube arrays was within the range 40–150 nm, and the thickness of the titanium and cerium oxide layer was assessed to be 10–25 nm. In order to calculate the average diameter, the transmission electron microscopy images were upsized by taking into account each nanotube section and subsequently averaging the measurement arrays. Different calcination temperatures were selected in the range 300, 500, and 700  $^{\circ}\text{C}$  to evaluate its effect on the morphological structure of the layer coating. Here, the nanocomposites exhibited a non-consolidated pattern characterized by a continuous and homogeneous layer of crystalline titanium and cerium oxides. Notwithstanding the disorganization that has been obtained for higher calcination temperatures, the layer covered the complete surface of the carbon nanotubes. Regarding the used nanocomposite samples, the TEM images showed an irregular presence of bare carbon nanotube arrays in  $\text{CNT}_{0.5}/(\text{TiO}_2)_9-(\text{CeO}_2)_{0.5}$ , thereby underlining the stability of the initial morphological structure, see Fig. 4bd. The effect of the calcination temperature was also derived from the occurrence of  $\text{TiO}_2$ - $\text{CeO}_2$  shells on the carbon nanotube matrix corresponding to the core region. This fact is somewhat ascribed to the titanium isopropoxide precursor that has been used to synthesize all  $\text{CNT}/\text{TiO}_2$ - $\text{CeO}_2$  nanocomposites. However, different precursors should be evaluated to query the influence of alkoxy groups on the morphology of the nanotube arrays. Particularly, the length of the alkyl chain and the steric configuration of the precursor were likely to affect the hydrolysis rate for titanium and cerium oxides.

### 3.4. XRD structure and chemical composition

The phase structure and composition of  $\text{CNT}/\text{TiO}_2$ - $\text{CeO}_2$  nanocomposites have been characterized by means of X-ray diffraction analyses. Fig. 5a and b shows the powder XRD patterns of

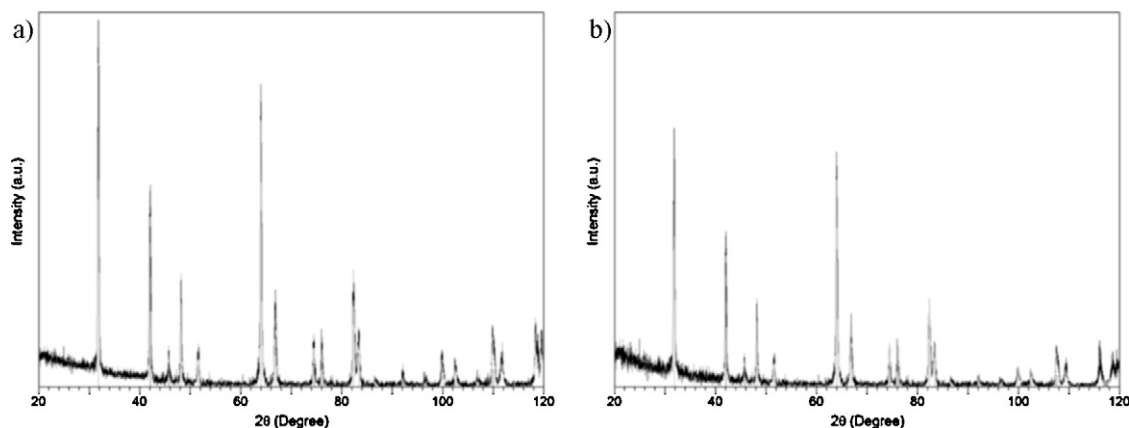
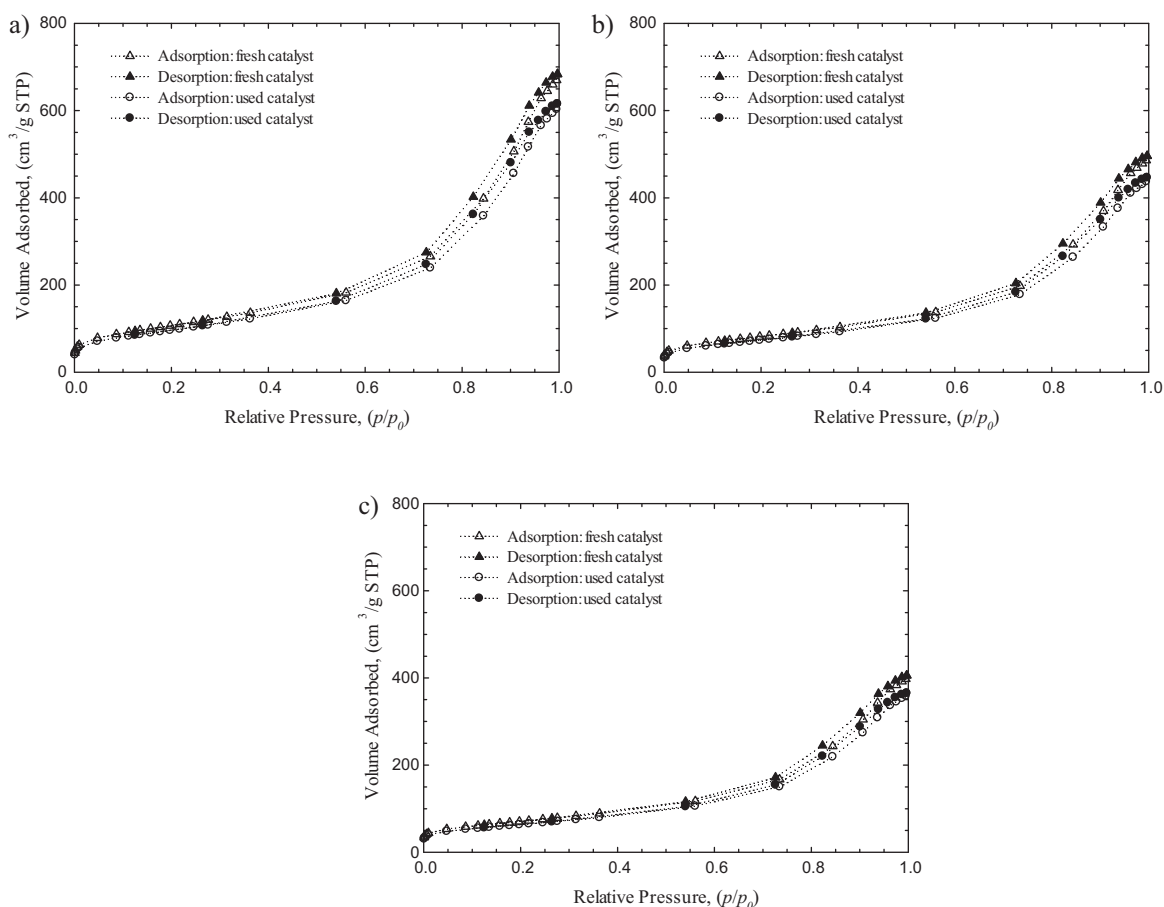


Fig. 5. X-ray diffractogram of (a) fresh and (b) used  $\text{CNT}_{0.5}/(\text{TiO}_2)_9-(\text{CeO}_2)_{0.5}$  nanocomposite.





**Fig. 6.** Brunauer–Emmet–Teller isotherm of fresh and used  $\text{CNT}_{0.5}/(\text{TiO}_2)_9-(\text{CeO}_2)_{0.5}$  catalyst for different calcination temperatures: (a) 300 °C, (b) 500 °C, (c) 700 °C.

the fresh and used  $\text{CNT}_{0.5}/(\text{TiO}_2)_9-(\text{CeO}_2)_{0.5}$ . As can be seen, the XRD diffractograms exhibited peaks at 40.5° and 53° which can be assigned to the titanium substrate. In fact, the XRD peaks at 25.3°, 37.6°, 49° and 55.5° are from the (1 1 0), (1 0 3), (2 0 0) and (1 0 5) diffractions, respectively, of anatase-phase titanium oxide. The representative diffraction peaks of  $\text{CeO}_2$  are 28.9°, 33.5°, 47.7°, and 56.6° from (1 1 1), (2 0 0), (2 2 0) and (3 1 1), respectively, as shown in Fig. 5. Both diffractograms demonstrate the crystal phase of the  $\text{CeO}_2$  so the lowest calcination temperature allows obtaining crystalline nanomaterials that were treated at 300 °C. In consideration of the calcination temperature influence, the carbon nanotubes that have been prepared without calcination maintained the original amorphous structure revealing a similar effect to the low-voltage anodization process. This route has been mostly generated amorphous  $\text{CNT}/\text{TiO}_2-\text{CeO}_2$  nanotubes; however it did not lead to the crystallization of titanium and cerium oxides. If one increases the calcination temperature without compromising the physicochemical stability of the carbon nanotube, amorphous regions have been progressively crystallized to generate anatase/rutile phases. Indeed, the XRD analysis unveiled that relative intensities of anatase and rutile diffraction peaks for the  $\text{CNT}/\text{TiO}_2-\text{CeO}_2$  nanocomposites are different for the titanium oxide layer under different calcination temperature. For temperatures lower than 300 °C, only a small diffraction peak of anatase at 25.3° was identified, while the rutile diffraction peaks were absent. This fact indicates that the phase rearrangement to anatase or rutile was not entirely attained below 300 °C and enclosed somewhat an inactive amorphous structure. Conversely, the treatment calcinations accomplished at 300 and 500 °C indicated typical XRD peaks at 25.3° (1 0 1), 27.5° (1 1 0), 36.3° (1 0 1), 48.2° (2 0 0), 54.5° (2 1 1),

and 69.6° (2 2 0). Additionally, the highest calcination temperature has been found to disintegrate the crystalline structure so the diffraction peak of anatase (1 0 1) vanished completely and the rutile peak (1 1 0) became considerably strong according to the XRD indexation at 700 °C. Therefore, the anatase phase was converted into the rutile one during heat cures at high calcination temperatures. Under these severe treatment conditions, the morphology of the nanotube structure partially collapsed by generating rutile crystallites with high densities.

### 3.5. BET and porosity analysis of nanocomposites

The BET isotherm for the  $\text{CNT}/\text{TiO}_2-\text{CeO}_2$  nanocomposites before and after 2 h of photocatalytic oxidation was determined through the accelerated surface area and porosimetry analyzer. Fig. 6a–c shows the Brunauer–Emmet–Teller isotherms for  $\text{CNT}_{0.5}/(\text{TiO}_2)_9-(\text{CeO}_2)_{0.5}$  prepared under different calcination temperatures. As can be seen, the increase in the cure temperature was found to diminish the volume absorbed for both fresh and used samples. The porosity analysis revealed quantitative differences in textural properties amongst the three samples by showing type IV isotherms. This behavior indicates the presence of mesopores in the nanoparticle matrix for the  $\text{CNT}/\text{TiO}_2-\text{CeO}_2$  composites. Table 1 shows the surface area and pore volume of CNT, pure  $\text{TiO}_2$  and  $\text{CNT}/\text{TiO}_2-\text{CeO}_2$  prepared with different molar proportions as well as the crystal sizes of  $\text{TiO}_2$  and  $\text{CNT}/\text{TiO}_2-\text{CeO}_2$  nanocomposites. The total pore volume was determined by the adsorption at a relative pressure of 0.995 for  $\text{N}_2$  at 77 K; and the  $d_{\text{TiO}_2-\text{CeO}_2}$  was the calculated  $\text{TiO}_2(-\text{CeO}_2)$  crystal size from XRD spectra of calcined catalysts. Here, the titanium and cerium oxides samples exhibited

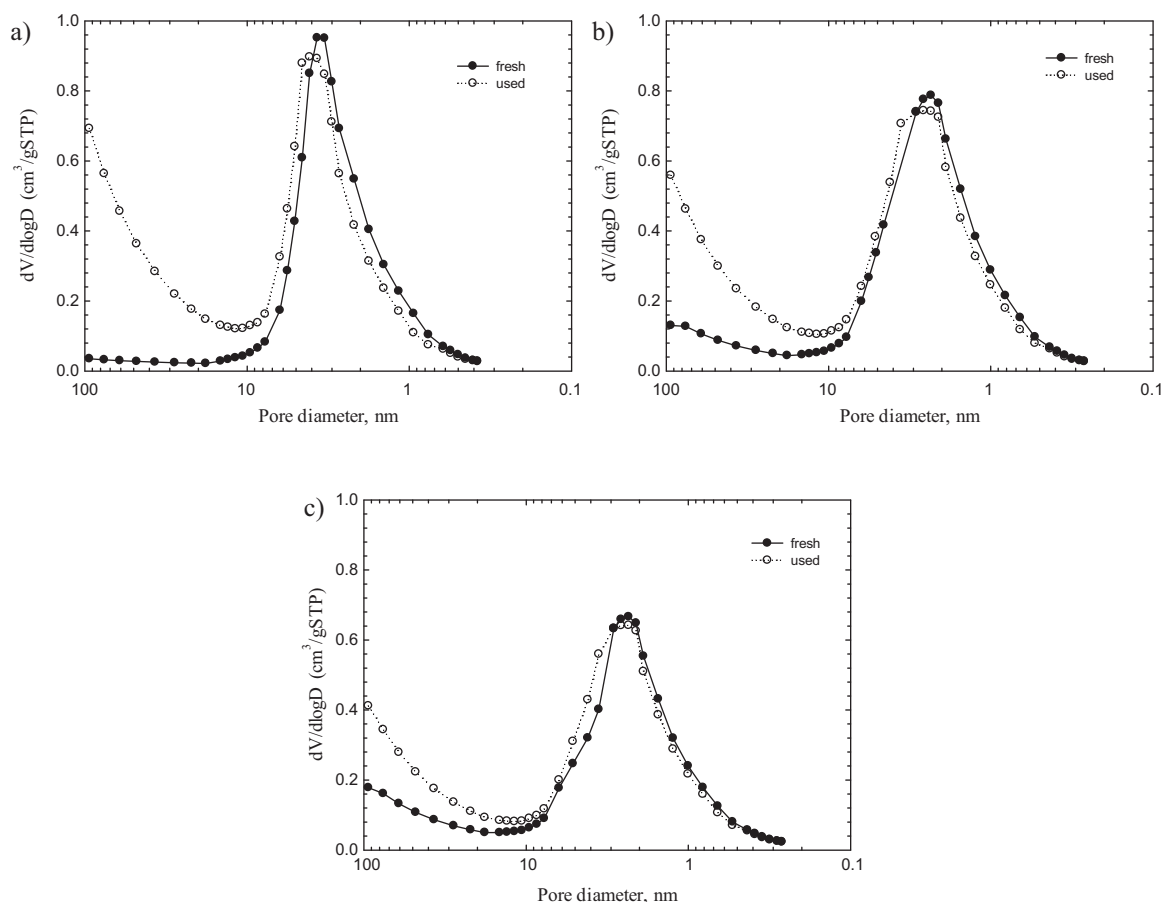


**Fig. 7.** Porosity size distribution of fresh and used  $\text{CNT}_{0.5}/(\text{TiO}_2)_9-(\text{CeO}_2)_{0.5}$  catalyst for different calcination temperatures: (a) 300 °C, (b) 500 °C, (c) 700 °C.

the lower surface areas and pore volume in comparison with that of pure carbon nanotubes. Table 1 indicates that the presence of a titanium oxide layer obstructed partially the initial carbon nanotube structure as well as somewhat clogged the nanotube array entrance. It is worthwhile to mention that the presence of carbon nanotube improved the textural properties of the  $\text{CNT}/\text{TiO}_2\text{--CeO}_2$  nanocomposites compared to pure  $\text{TiO}_2$  and  $\text{CeO}_2$  aggregated particles, by guarantying an exposed assembly of the nanotube array and high surface area support for the growth of the  $\text{TiO}_2\text{--CeO}_2$  film.

Fig. 7a–c plots the pore size distribution of the multiwall carbon nanotube composite with titanium and cerium oxides. The most active catalyst  $\text{CNT}_{0.5}/(\text{TiO}_2)_9-(\text{CeO}_2)_{0.5}$  exhibited reasonable differences concerning the effect of the calcination temperature. Both fresh and used samples have slightly narrow pore size distribution profiles at lower cure temperatures and became wider as the calcination temperature increases. The reduction of surface area after calcination can be ascribed to the contraction of the porous coating mainly due to the heat-induced crystallization.

**Table 1**  
Brunauer–Emmet–Teller surface area ( $S_{\text{BET}}$ ) and pore volume of CNT, pure  $\text{TiO}_2$  and  $\text{CNT}/\text{TiO}_2\text{--CeO}_2$  prepared with different molar proportions; crystal sizes of  $\text{TiO}_2$  and  $\text{CNT}/\text{TiO}_2\text{--CeO}_2$  nanocomposites.

	$(S_{\text{BET}}) (\text{m}^2/\text{g}^{-1})$	$V_{\text{pore}} (\text{cm}^3 \text{g}^{-1})$	$d_{\text{TiO}_2-(\text{CeO}_2)} (\text{nm})$
CNT	258	2.37	
$\text{TiO}_2$	188	0.16	12.6
$\text{CNT}_1/(\text{TiO}_2)_9$	247	0.39	3.9
$\text{CNT}_2/(\text{TiO}_2)_7-(\text{CeO}_2)_1$	264	0.21	3.2
$\text{CNT}_1/(\text{TiO}_2)_8-(\text{CeO}_2)_1$	241	0.43	2.8
$\text{CNT}_{0.5}/(\text{TiO}_2)_9-(\text{CeO}_2)_{0.5}$	229	0.33	3.1

From the tabulated data, the  $\text{CNT}/\text{TiO}_2\text{--CeO}_2$  composites had analogous properties notwithstanding the higher surface area and lower pore volume compared to pure  $\text{TiO}_2$ . The larger crystal size is probably due to the more condensed structure of titanium oxide shell, which can be emphasized by the rough differences in the coating thickness and morphological structure detected in the TEM patterns, see Fig. 4. Consequently, the  $\text{TiO}_2$  had larger crystal sizes comparatively to the crystals of  $\text{CNT}/\text{TiO}_2\text{--CeO}_2$  nanocomposites due to the spatial arrangement of the carbon nanotube scaffold leading to larger BET surface areas.

### 3.6. Long-term catalytic activity

Apart from the physicochemical characterization techniques used to characterize the  $\text{CNT}/\text{TiO}_2\text{--CeO}_2$  nanocomposites, particular attention was focused on how the  $\text{CNT}_{0.5}/(\text{TiO}_2)_9-(\text{CeO}_2)_{0.5}$  catalyst preserves the removal efficiency in terms of total organic carbon. The normalized TOC concentration of five sequential feed-batch catalytic runs is illustrated in Fig. 8 at  $T=25^\circ\text{C}$  and UV-254 nm. A benchmark parameter was to carry out the catalyst reuse during several hours of photocatalytic mineralization. In this regard, the above-selected nanocomposite was recycled along consecutive feed-batch trials to quantify if the mineralization efficiencies remained at analogous conversions or if it is adversely affected on the photocatalytic activity. Systematic injections after two hours of reaction time of a pre-determined phenol-like pollutants solution were carried out in order to obtain a concentration close to the starting value. As can be seen, the photo-oxidation conversions after 10 h operating time almost kept the detoxification rate. Notwithstanding the BET surface area decreased slightly from



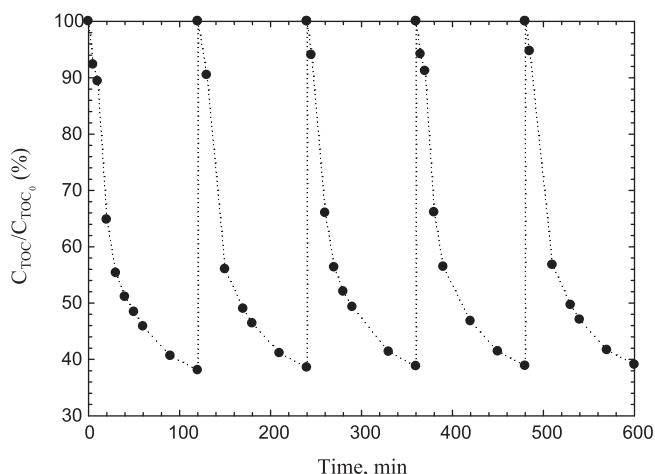


**Fig. 8.** Normalized total organic carbon concentration as function of time for a sequential batch experiment with phenolic mixture injection each 120 min.

229 to 222  $\text{m}^2/\text{g}$ , the mineralization rate in terms of total organic carbon concentration was roughly the same during the five successive experimental runs. Likewise, the  $\text{CNT}_{0.5}/(\text{TiO}_2)_9-(\text{CeO}_2)_{0.5}$  nanocomposite consecutively exhibited higher detoxification rates during the first hour of each oxidation experiment. Indeed, the photodegradation rate has been kept at 61% for all catalytic feed-batch trials.

#### 4. Conclusions

Carbon nanotubes and pure  $\text{TiO}_2$  are not able to mineralize efficiently phenol-like pollutants. In this regard, several  $\text{CNT}/\text{TiO}_2\text{--CeO}_2$  nanocomposites have been prepared with different molar proportions to photodegrade the organic content of agro-industrial wastewaters. The photocatalytic activity in terms of parent compound conversion and total organic carbon depletion has revealed that the  $\text{CNT}_{0.5}/(\text{TiO}_2)_9-(\text{CeO}_2)_{0.5}$  nanocomposite gave detoxification rates higher than 88 and 60%, respectively. Field emission scanning electron microscopy photographs have revealed a highly heterogeneous porous structure with similar nanotube lengths for a thicker wall of  $\sim 100$  nm. A continuous layer of  $\text{TiO}_2$  and  $\text{CeO}_2$  coating the entire surface of the carbon nanotubes was identified in the transmission electron microscopy patterns. Additionally,  $\text{TiO}_2\text{--CeO}_2$  shells were found on the carbon nanotube matrix corresponding to the core region, which has been attributed to the titanium precursor that was used to synthesize all  $\text{CNT}/\text{TiO}_2\text{--CeO}_2$  nanocomposites. The effect of the calcination

temperature was subsequently evaluated in XRD structure analyses so the catalysts that have been obtained without calcination maintained the original amorphous structure and crystallized differently as the temperature increases till  $700^\circ\text{C}$ . Furthermore, the BET and porosity analysis of fresh and used nanocomposites unveiled mesoporous morphologies for the carbon nanotube arrays. Both fresh and used specimens have exhibited narrow pore size distribution profiles at lower calcination temperatures and became wider as the cure temperatures become higher than  $500^\circ\text{C}$ . From a long-term performance viewpoint, the  $\text{CNT}_{0.5}/(\text{TiO}_2)_9-(\text{CeO}_2)_{0.5}$  catalyst was reutilized during five photo-oxidation runs exhibiting practically the same pollutant removal efficiencies, thereby presenting an efficient nanocomposite for the environmental detoxification of phenolic wastewaters.

#### Acknowledgment

The authors gratefully acknowledged the financial support of *Fundação para a Ciência e Tecnologia*, Portugal.

#### References

- [1] M. Pera-Titus, V. García-Molina, M.A. Baños, J. Giménez, S. Esplugas, *Applied Catalysis B: Environmental* 47 (2004) 219–256.
- [2] F.J. Rivas, M. Carbajo, F. Beltrán, O. Gimeno, J. Frades, *Journal of Hazardous Materials* 155 (2008) 407–414.
- [3] P. Cañizares, J. Lobato, R. Paz, M.A. Rodrigo, C. Sáez, *Chemosphere* 67 (2007) 832–838.
- [4] P. Paraskeva, E. Diamadopoulos, *Journal of Chemical Technology & Biotechnology* 81 (2006) 1475–1485.
- [5] A. Mandal, A.K. De, S. Bhattacharjee, *Chemical Engineering Journal* 102 (2004) 203–208.
- [6] S. Esplugas, J. Giménez, S. Contreras, E. Pascual, M. Rodríguez, *Water Research* 36 (2002) 1034–1042.
- [7] C.Y. Kuo, *Journal of Hazardous Materials* 152 (2008) 949–954.
- [8] N. Serpone, P. Maruthamuthu, P. Pichat, E. Pelizzetti, H. Hidaka, *Journal of Photochemistry and Photobiology A* 85 (1995) 247–255.
- [9] J.C. Yu, L.Z. Zhang, J.G. Yu, *New Journal of Chemistry* 26 (2002) 416–420.
- [10] H. Yahiro, T. Miyamoto, N. Watanabe, H. Yamaura, *Catalysis Today* 120 (2007) 158–216.
- [11] H.H. Patterson, R.S. Gomez, H. Lu, R.L. Yson, *Catalysis Today* 120 (2007) 168–173.
- [12] P. Li, G. Zhao, M. Li, T. Cao, X. Cui, D. Li, *Applied Catalysis B: Environmental* 111–112 (2012) 578–585.
- [13] V. Jaeger, W. Wilson, V. Subramanian, *Applied Catalysis B: Environmental* 110 (2011) 6–13.
- [14] B. Abida, L. Chirdi, S. Baranton, T. Napporn, H. Kochkar, J. Léger, A. Ghorbel, *Applied Catalysis B: Environmental* 106 (2011) 609–615.
- [15] T.W. Ebbesen, H.J. Lezee, H. Hiura, J.W. Neentt, H.F. Ghaemi, T. Thio, *Nature* 382 (1996) 54–56.
- [16] Y. Yu, J.C. Yu, C.Y. Chan, Y.K. Che, J.C. Zhao, L. Ding, W.K. Ge, P.K. Wong, *Applied Catalysis B* 61 (2005) 1–11.
- [17] X.Z. Li, F.B. Li, C.L. Yang, W.K. Ge, *Journal of Photochemistry and Photobiology A: Chemistry* 141 (2001) 209–217.
- [18] Y. Yu, J.C. Yu, C.Y. Chan, Y.K. Che, J.C. Zhao, L. Ding, W.K. Ge, P.K. Wong, *Applied Catalysis A* 289 (2005) 186–196.